Title
Elastomeric sensor surfaces for high-throughput single-cell force cytometry.

Journal
Nature biomedical engineering, 2(2)

ISSN
2157-846X

Authors
Pushkarsky, Ivan
Tseng, Peter
Black, Dylan
et al.

Publication Date
2018-02-01

DOI
10.1038/s41551-018-0193-2

Peer reviewed

HHS Public Access

Author manuscript

Nat Biomed Eng. Author manuscript; available in PMC 2019 July 10.

Published in final edited form as:

Nat Biomed Eng. 2018 February ; 2(2): 124–137. doi:10.1038/s41551-018-0193-2.

Elastomeric sensor surfaces for high-throughput single-cell force biology

Ivan Pushkarsky[*],
Department of Bioengineering, University of California, Los Angeles

Peter Tseng[*],
Department of Bioengineering, University of California, Los Angeles

Lyndon Warfe,
Department of Bioengineering, University of California, Los Angeles

Dylan Black,
Department of Bioengineering, University of California, Los Angeles

Bryan France,
California NanoSystems Institute, University of California, Los Angeles

Cynthia J. Koziol-White,
Rutgers Institute for Translational Medicine and Science, Child Health Institute, Rutgers University, New Brunswick, New Jersey, United States

William F. Jester Jr.,
Rutgers Institute for Translational Medicine and Science, Child Health Institute, Rutgers University, New Brunswick, New Jersey, United States

Ryan K. Trinh,
Department of Microbiology, Immunology and Molecular Genetics and The Molecular Biology Institute, University of California, Los Angeles

Jonathan Lin,
Department of Bioengineering, University of California, Los Angeles

[**]corresponding author.

Author contributions

I.P. and P.T. contributed equally to this work. P.T and D.D. and I.P. conceived the method. I.P., R.D., P.O., S.M., R.P., C.J.K and D.D. designed experiments. I.P. performed all experiments, developed the multi-well embodiment, optimized protocols, and wrote the image analysis software. D.B. assisted in substrate preparation and macrophage differentiation procedures. L.W. assisted with substrate fabrication. R.T. maintained chimeric antibody stocks. S.M. supplied all chimeric antibodies. J.L. constructed the finite element method model. R.D. supplied HTS equipment for dose-response experiments and provided technical advice on HTS procedures and on developing the multi-well plate embodiment. B.F assisted with HTS equipment and drug administration. W.J. maintained donor HASM cells. P.O. performed MDC differentiation and advised experimental procedures. I.P., R.D., P.O., S.M., R.P., C.J.K and D.D. interpreted the results. I.P. and D.D. wrote the manuscript. R.D., P.O., S.M., R.P., C.J.K helped revise the manuscript.

[*]equally contributed as authors

Competing financial interests

I.P., P.T., and D.D. are named inventors on a patent application by the University of California, Los Angeles that covers the technology described. I.P., R.D. and D.D. have a financial interest in Forcyte Biotechnologies, Inc. which aims to commercialize FLECS technology.

Data Availability

The data and that support the findings of this study, along with the algorithms used for image analysis are available from the corresponding author upon reasonable request.

Philip O. Scumpia,
Division of Dermatology, David Geffen School of Medicine, University of California, Los Angeles

Sherie L. Morrison,
Department of Microbiology, Immunology and Molecular Genetics and The Molecular Biology Institute, University of California, Los Angeles

Reynold A. Panettieri Jr.,
Rutgers Institute for Translational Medicine and Science, Child Health Institute, Rutgers University, New Brunswick, New Jersey, United States

Robert Damoiseaux, and
Department of Molecular and Medicinal Pharmacology, University of California, Los Angeles

California NanoSystems Institute, University of California, Los Angeles

Dino Di Carlo[**]
Department of Bioengineering, University of California, Los Angeles

Department of Mechanical Engineering, University of California, Los Angeles

California NanoSystems Institute, University of California, Los Angeles

Abstract

All cell types generate mechanical forces in the contexts of their single-cell or tissue-level physiological roles. Since aberrant force-generating phenotypes directly lead to diseases, cellular force-generation mechanisms are high-value targets for new therapies. We report a scalable microtechnology to embed single-cell force sensors into elastomers that seamlessly integrates with the multi-well plate format to leverage laboratory automation workflows and achieves ~100-fold improvements in throughput for single-cell force measurements. We perform highly-parallelized time-course studies investigating airway biology and show that airway smooth muscle cells isolated from fatally asthmatic patients exhibit innately greater, and more rapid force generation in response to agonist than non-diseased cells. By also simultaneously tracing agonist-induced calcium flux and contractility in the same single cells, we reveal that calcium level is ultimately a poor quantitative predictor of cellular force generation. Finally, our flexible bio-functionalization approach uniquely enabled quantification of phagocytic forces in 1,000s of individual human macrophages and revealed that initiation of this force is a digital rather than a proportional response to the proper immunogen.

Introduction

Cell-generated mechanical forces, which normally fulfill essential biological roles at both the cellular level (mechanotransduction[1], migration[2], cytokinesis[3], immune processes[4], vasoregulation[5]) and tissue level (tone maintenance, concerted contractions) can at times become dysregulated leading to diseased anatomical states or loss of function. Abnormally high force generation underlies bronchoconstriction[6] in asthma, hypertensive vasoconstriction and stroke[7], muscle spasms, and is also involved in fibrotic tissue stiffening[8] and in the pathogenesis of cancer[9]. Conversely, cells' inability to generate force

describes the phenotypic basis for cardiac insufficiency and congenital defects such as X-linked neutropenia and muscular dystrophy. Undesired vasodilation in the brain has also been noted as the physiological trigger for migraine pain[10]. Thus, cellular force generation can serve as a useful measure to evaluate disease state and provides a valuable therapeutic target.

For several therapeutic indications, existing treatments promote relaxation of cell shortening through established molecular pathways. However, the coupling of the molecular pathways to the contractile force remains poorly understood. Since conventional therapies induce severe side-effects, tolerance development or simply are ineffective, new approaches are needed that act specifically and effectively on mechanical force transduction. A scalable, general-use cellular force cytometer that could rapidly evaluate large screening libraries – and identify such candidates - has the potential to accelerate drug development efforts and anchor research in force biology.

Existing techniques for performing these measurements suffer from strict trade-offs between quality of data on the one hand, and throughput and ease-of-use on the other. Traction force microscopy (TFM)[11,12] and elastomeric micropost array (EMA)[13] assays can resolve subcellular forces but require laborious manual steps that have limited throughput to only a few dozen cells in a typical experiment[14–17]. TFM serially implemented in a microtiter plate format increased throughput but lost its single-cell resolution, instead reporting a noise-prone, bulk “response-ratio” measurement[11] that overlooks clinically important subpopulations, such as the highly contractile platelets present in patients with normal clotting function[18]. A concept combining TFM and fluorescent micropatterns was also proposed but was ultimately limited to proof–of-principle due to practical fabrication challenges[19]. To address the need to scale up data acquisition both in terms of cell numbers and temporal resolution, we introduce an integrated biosensor material comprised of fluorescently-labeled elastomeric contractible surfaces (“FLECS”) for making single-cell force measurements at throughputs ~100-fold higher than previously possible.

In the FLECS system, each cell adhering to one of thousands of uniform adhesive and fluorescent micropatterns generates comparable mechanical forces onto the underlying elastomeric film, and produces unique, well-calibrated displacements at their respective micropatterns’ peripheries (Fig. 1A, Movies S1, S2), which can be easily quantified using image analysis algorithms (Fig. 1C). By combining microcontact printing of proteins with sacrificial layers, we can stably encode micropatterns consisting of *any* biomolecule bearing free amine or thiol groups into a silicone elastomer without using costly linkers -- resulting in uniform micropatterns that are unaffected by material stiffness (Fig. S1). This allows us to simulate diverse tissue environments which, in turn, can elicit a wide range of measurable force-generating behaviors, from basal smooth muscle tone to phagocytosis. Importantly, in a multi-well plate format, FLECS achieves a substantial degree of parallelization without linear increases in fabrication labor. The 96-well plate embodiment (containing >6000 70 μm “X” patterns per well) is natively compatible with existing automation and screening infrastructures, i.e. liquid handling robotics, plate handling robotics and high-content imaging systems, and offers a practical solution to performing highly-parallelized assays and other general experiments that were previously too costly or cumbersome.

Results

Whole-cell contractility measurements resolve population-wide contractile differences

FLECS provides whole-cell contractility measurements. To show that this level of resolution is sufficient for detecting population-wide contractile differences, we assayed human multipotent mesenchymal stem cells (hMSCs), which are known to exert large contractile forces and interrogate mechanical cues in their environment[20,21], and their differentiated progeny. HMSCs spread uniformly to occupy 70 micron fibronectin “X” patterns, forming dense actin stress fibers (Fig. 2B and Fig. S3). Regardless of tissue of origin, hMSCs in a multipotent state produced significantly higher steady-state micropattern displacements, suggesting greater force generation, than either set of differentiated hMSCs (Fig. 2A). Previously, Fu *at al.* demonstrated high forces in differentiating hMSCs that peaked in the first day of culture but declined over the following 7 days[22]. Our results support this earlier conclusion as they reveal significantly lower forces in MSCs following longer differentiation times (i.e. at 14 days as in our experiment), and indicate that subcellular resolution is not necessary for population-wide cellular force cytometry. Furthermore, because FLECS assays all cells present in a sample without pre-selection in one automated procedure, we obtained data for 180 to >1500 cells per condition (rather than 13–62 cells as was presented in the previous study) and identified a smaller sub-population of weakly contractile cells in each multipotent stem cell sample.

Additional experiments using FLECS were performed to characterize and compare whole-cell contractility for three types of primary human smooth muscle cells (SMCs) —bronchial SMCs (BSMCs), aortic SMCs (ASMCs) and uterine SMCs (USMCs). These cells were observed to uniformly spread over and contract thousands of 70 μm “X” patterns, producing measurable displacements which were on average greater for ASMCs and USMCs than for BSMCs, suggesting higher native force generation by those cells in the absence of stimuli (Fig. S4). A larger subpopulation of weakly contracting cells was also identified in the USMC distribution, perhaps due to the relative difficulty of isolating pure populations from this complex tissue. These experiments further support the suitability of FLECS for studying the force biology of a variety of adherent tissue cells.

Considering the multitude of disorders arising from abnormal SMC contractility including asthma, hypertension, and bowel disease[23], a tool for rapid force-phenotyping of large SMCs populations would be invaluable for research and drug development purposes. In support of this idea, we tested whether whole-cell contractility measurements obtained with FLECS provide sufficient resolution for performing functional phenotypic screens of modulators of cellular force, and if accurate quantitative characterization of drug compounds can be achieved. To do so, we titrated the myosin II inhibitor, blebbistatin, using contracting primary airway smooth muscle (HASM) following a 10-step, 2-fold dilution scheme and vehicle controls with 4 technical replicates for each (equating to 44 independent measurements) on a single functionalized 96-well plate (Fig. 2C). As expected, addition of this tool compound produced a restorative effect on the cell-contracted micropatterns (Movie S3), which was dose-dependent. We observed low variability across replicates and calculated an IC_{50} of 2.61 μM which matches previously reported values[24,25] (Fig. 2D). These results

show that automating (and scaling) the FLECS assay is feasible and yields robust readouts. As such, we expect the FLECS well-plate will facilitate automated screens of large drug libraries to help identify new candidates for correcting malfunctioning cellular contractility. The single-cell resolution should also help reveal any non-Gaussian responses to modulators at the population level.

Airway smooth muscle cells isolated from donors with asthma inherently generate higher forces

Used together with laboratory automation equipment, the well-plate implementation of FLECS provides new opportunities to perform highly parallelized and multi-faceted studies of force generation with high precision and fine temporal resolution. Here, we harnessed these capabilities to thoroughly evaluate the functional contractile profiles of primary human airway smooth muscle (HASM) cells isolated from patients with fatal asthma and compare them to cells from patients who were age-, race-, and gender-matched without asthma. Researchers in the field have supposed that innate differences in force generation should exist between the two sets yet the various aspects of this phenotype have never been compared directly using a single method or with large quantities of cells. Although a previous study compared this mechanophenotype between patient cells using TFM for a number of cells at baseline, the traction moments were not normalized to cell-spread area which is known to dictate traction forces, and contractility could not be assessed following dosing with agonists[26]. Moreover, the comparative responsiveness to asthma treatments has not previously been compared between normal and diseased HASM cells. Here, we aimed to provide a definitive report on whether force generation was indeed inherently greater in asthma HASM using a single measurement platform and evaluating both tone and responsiveness in 1000s of the same cells. For this study, i) we evaluated basal cell tone, ii) contractile responsiveness to treatment with a bronchoconstrictor, and iii) responsiveness to attempted rescue from bronchoconstriction using the asthma standard-of-care β2-adrenoceptor agonist formoterol in the same cells, using 6 unique patient samples from each group (Fig 3).

HASM cells from asthmatic patients contracted patterns with a higher baseline tone than cells from healthy patients. To first evaluate tone, the 12 HASM cell lines were seeded into 8 wells each within three FLECS multiwell plates, each of which was assembled with independently mixed batches of silicone elastomer. Following adhesion and serum-starvation, all wells were imaged to obtain basal (tonic) contraction levels for the 12 cells lines. The trends in tonic contraction between the 12 cell populations were conserved across the three samples, and the minor inter-well-plate variability was significantly less than the inter-donor variability we observed, indicating the method reliably discerns biological differences (Fig. S5). Here, we observed that, the asthma HASM exhibited, on average, higher tone than non-asthma HASM. When compared as two pooled groups, the median basal tone of all asthma HASM were statistically greater than the median basal tone of non-asthma HASM (Fig. 3E).

Immediately after imaging cells in their tonic contracted state, we treated all cells with the contractile agonist bradykinin (BK) at a final concentration of 10 μM. We had previously

observed bradykinin as well as endothelin-1, both molecules that have been impugned in asthma, to promote significant contraction in primary HASM (Movies S4, S5). Following treatment, all 96 sites were re-imaged once every 4 minutes for 16 minutes, at which point the plate was removed from the imager and half the wells received 50 μM formoterol, and the other half received vehicle (1% DMSO). The plate was replaced and all sites were imaged for another 20 min at 4 min intervals, before a final time-point was recorded 10 min later. Contractility for each of the ~31,000 cells was tracked over time and cells exhibiting increased contraction at 16 min relative to baseline were selected for further analysis (~72% of cells on average).

We tracked the evolving contractile distributions for all selected cells (Fig. 3B) and found the distributions showed robust upward shifts following treatment with BK that were un-attenuated following addition of vehicle, but were halted or reversed following treatment with formoterol. The median contractility value of each cell population was tracked over the course of pharmacological treatment (Fig. 3C) and it was observed that for 5 out of 6 pairs of age-, race-, and gender- matched patients with or without fatal asthma, the asthmatic patients' cells exhibited either greater tone, greater BK-induced contraction, or both (Fig 3D). In 4 of these cases, the differences were statistically significant. One asthma line (asthma patient #6) displayed lower contraction in all respects than its healthy patient counterpart. We conclude that, in general, HASM isolated from fatal asthma patients innately generate greater force than cells isolated form their healthy counterparts.

Acute contractile response to agonist also appeared significantly accelerated in fatal asthmatic patient-derived cell lines. Specifically, the initial rates of contractile response, defined as the change between the initial tonic reading and first measurement following BK-stimulation, were greater in asthmatic lines than in normal ones and this difference in rate was statistically significant (Fig. 3E). Interestingly, despite this initial differential response, which was observed out to 3 imaging time-points, or roughly 12 mins (not shown), the total increase over the full course of the experiment was similar between the groups. This indicated that while there are clearly differences in absolute force generation between asthma and normal lines, the differences in their relative responsiveness to agonists may be dominated by kinetics. Finally, we assessed whether rescue by formoterol was differentially effective among the two groups. Traces of the population medians (Fig. 3C) indicated that a number of cell lines from both groups showed substantial reversal following treatment with formoterol., but both groups also had cells responding more asymptotically. Accordingly, when compared collectively, the asthma and normal human airway smooth muscle cell lines manifested similar responsiveness to formoterol. However, a subset of normal-derived cell lines showed substantially greater reversal than any asthma-derived lines (Fig. 3E).

Conventional calcium release assays poorly predict functional contractility in HASM

Using the FLECS workflow, cells may be imaged live or fixed in their contracted state and subsequently phenotypically profiled. Since the cells are confined to micropatterns with known positions and boundaries, a simple algorithm can be used to quantify molecular biomarkers associated with a functional output (e.g., contraction) at the single-cell level over

a population of cells. We applied this analysis to address the correlation in agonist-induced increases in cytosolic calcium with contraction responses in HASM in a cell-by-cell manner.

Excitation-contraction coupling of HASM requires the highly coordinated activation of calcium mobilization pathways with released calcium from intracellular calcium stores and with calcium influx from the extracellular space. Calcium sensitization activates rho kinase to inhibit myosin light chain phosphatase activity and activate actin polymerization and reorganization pathways, as well as enable myosin-actin interaction. Some but not all of these pathways are calcium dependent and no techniques have previously been demonstrated to distinguish the relative contribution of calcium mobilization with simultaneous measurements of force generation in single-cells. Here, by first recording changes in calcium-sensitive dye intensities within HASM arrayed on a FLECS well-plates (Movie S6) and then monitoring the changes in their respective micropatterns (Fig. 4A–B), we show that the magnitude of agonist-induced peak calcium and HASM contraction responses are differentially modulated by agonists.

Comparing agonist-induced peak calcium and contraction responses in 100s of HASM single-cells, on average, BK and histamine (Hist) manifested the greatest calcium responses whereas the greatest contraction responses were observed with serum and ET-1 stimulation (Fig. 4C). Interestingly, at the single-cell level there were no correlations among peak calcium and maximal contraction for any tested agonist, even when the populations were gated to only include responders (e.g. cells exhibiting either >1 μm contraction increases or > 1.1 fold-change in calcium dye intensity; Fig 4D, Fig. S6). In fact, some high calcium responders manifested no contraction, while some very weak calcium responders produced substantial contractile responses. Some of these effects may be explained by activation of receptors differentially coupled to G proteins. For example, histamine activates the Histamine 1 receptors that is coupled to Gq that increases phospholipase β that then activates the canonical IP3 pathway. Histamine however also activates the Histamine 2 receptors coupled to Gs that then increases cAMP and activates protein kinase A that antagonizes force generation. The net effect on histamine-induced force generation will likely relate to the stoichiometry of the differential receptor activation. Similarly, serum that contains a variety of agonists will likely activate a multitude of HASM receptors that have differential effects on calcium mobilization and force generation.

Collectively, our data supports the hypothesis that agonist-induced peak calcium responses may not correlate with force generation, and that while calcium release assays may generally indicate contractile pathways have been activated, they have limited usefulness as a quantitative predictor of cellular contractility. These findings suggest that high-throughput screens of force modulators using calcium sensitive dyes, as have been recently suggested[27] may have significant limitations in terms of specificity and predictivity. Overall, we demonstrate that FLECS allows unique multi-modal studies involving contractility and to be performed on single cells *in situ*, including transient biological events occurring on sub-minute timescales. As with all previous experiments, we achieved relatively large N for all experimental conditions, and all present cells were evaluated automatically by the algorithm. By simultaneously addressing functional and molecular phenotypes in large numbers of cells

using automation, FLECS presents new opportunities to discriminate between modes of actions of biological agonists associated with abnormal contractility diseases.

Force generation in phagocytosis acts in a digital manner

In innate immunity, mechanical forces direct phagocytosis – the process by which phagocytes internalize and destroy foreign pathogens and clear cellular debris. Operating at the single-cell level, our new tool is uniquely suited to evaluate phagocytic forces in individual primary human macrophages, a measurement that has not been previously demonstrated. We achieved this by embedding dansylated bovine serum albumin (DNS-BSA) micropatterns into the elastomeric surface, and incubating them with anti-dansyl chimeric IgG (hIgG). The resultant micropatterned immune-complexes reliably promoted a phagocytic response: human monocyte derived macrophages (MDMs) rapidly adhered, spread over, and contracted the opsonized patterns and maintained the contraction for up to 16 hours (Fig. 5A–B, Movie S7).

We first investigated the open question of whether the quantity of presented stimulus modulates total phagocytic force. This was done by patterning hIgG into three equi-diametric circular shapes (to control cell-spread area) but with different interior geometries to vary the quantities of presented antibody. The MDMs spread uniformly over micropatterns of each shape and, surprisingly, produced statistically similar micropattern displacements (Fig. 5C). This result suggests that, like the triggering of cytokine secretion in T cells[28], the phagocytic pathway leading to force generation acts in a digital manner, turning “on” completely at a certain threshold, but not scaling with opsonin quantity.

We expected that forces involved in FcR-mediated phagocytosis would exceed less biologically urgent forces initiated by other adhesive opsonins. To evaluate this, we also examined MDM responses to non-opsonized DNS-BSA as well as fibrinogen (Fg) or vitronectin (Vn) -- molecules that support long-term macrophage adhesion but have less understood immunological roles[29,30]. Micropatterns with hIgG presented with the largest displacements while micropatterns with Fg, Vn, and DNS-BSA generally presented with very minute displacements, supporting our hypothesis. However, for each of these three other conditions, there was a small subpopulation of MDMs that did apply substantial contractile forces, comparable to hIgG (Fig. 5D). We suppose this is because a subset of the MDMs, which were initially differentiated from a heterogeneous pool of monocytes[31], have become activated by these molecules through interactions with other (non-FcR) receptors, ultimately converging in downstream signaling pathways leading to phagocytosis -- further supporting the notion that phagocytic force generation acts in a digital manner.

Macrophages generate hundreds of nanonewtons of force during phagocytosis

Using finite element method (FEM) solid mechanics modeling based on the micropattern displacements and mechanical properties we measured for the material, we approximated the forces applied onto the micropatterns. We found that MDMs engaged in FcR-mediated phagocytosis generated median forces of ~350 nN while a number of outlier cells were capable of forces as large as 1 μN (Fig. 5D–E). Median forces generated by MDMs on the other opsonins were significantly less, never exceeding 100 nN. Forces in the 10^{-7} N range

have previously been reported for other human cells including MSCs, HUVECs[22], and keratinocytes[32]. Phagocytic forces in this range should be expected as the adhesive strengths of certain bacteria were also found to approach the μN range[33]. It is also interesting to note that the macrophages generated similar levels of force on both substrates despite difference in their stiffnesses, since a previous study reported correlation between forces in migrating macrophages and substrate stiffness[34]. The lack of such relationship here is likely due to the difference in behavior that is being analyzed. Specifically, while there may be physiological reasons for more rapid migration on stiffer surfaces, there does not appear to be a benefit to modulating phagocytic force if the objective is rapid clearance of a foreign entity. Moreover, it is possible that the response is only linear on the small range of stiffnesses we tested (4kPa – 8 kPa), and that it may behave differently over a larger range. Overall, this analysis represents the first direct quantification of the contractile forces involved in the closure of the phagocytic cup.

Subclasses of IgG stimulate similar phagocytic force generation

A recent study reported minor differences in the ability of different IgG subclasses to stimulate phagocytic uptake of *Salmonella* bacterial cells by a monocytic cell line[35]. We asked whether these differences were triggered at the force-generation level. Using a humanized panel of the four subclasses of IgG antibodies we found that all subclasses induced significant and comparable increases in phagocytic force over the non-opsonized controls. We observed a similar result for another phagocyte, matched immature monocyte-derived dendritic cells (MDDCs) derived from the same patient (Fig. S7). It is not entirely surprising that MDMs and MDDCs produced similar forces since both are professional phagocytes with the same general targets e.g. bacteria, parasites, debris. However, these results suggest that if phagocytic uptake efficiency does indeed differ among the subclasses, it is not a result of differences in force-generation.

Pharmacological inhibition of actin polymerization but not of phagosome acidification reduces phagocytic force

Actin polymerization has long been known to be required for phagocytosis, with target uptake assays showing that actin inhibitors greatly reduce phagocytic efficiency, particularly with Fc-opsonized targets[36]. Given its role in phagosomal closure, it is logical that inhibition of polymerization would reduce phagocytic force. Following closure, the internal phagosomal pH progressively decreases, enhancing its microbicidal activity[37]. It remains unknown whether there is feedback between phagosome maturation and the sustained maintenance of a phagocytic force.

We used FLECS to both confirm direct role of actin polymerization in phagocytic force and also to determine whether disruption of phagosomal acidification (a late-stage event) fed back into the control of the earlier mechanical stages of phagocytosis. We treated MDMs with cytochalasin D or chloroquine at three doses to block actin polymerization or phagosomal acidification, respectively. MDMs were either seeded directly into drug-containing medium or incubated with drug after achieving steady-state phagocytic contraction on hIgG “X” patterns. As expected, incubation with cytochalasin D at all tested doses substantially decreased the measured phagocytic contraction, while pre-treatment

completely prevented any measureable contraction, confirming the requirement of actin polymerization in phagocytic force generation (Fig. 6A–D). Treatment with chloroquine had no effect on the mechanical output of the macrophages, indicating the early-stage mechanical encapsulation and chemical maturation involved in phagocytic clearance are uncoupled in both the long-term and short-term.

PI3K inhibition reduces the forces generated during FcR-mediated phagocytosis

Finally, we investigated the role of a specific phosphatidylinositide 3-kinase (PI3K) isoform, p110δ, in phagocytic force. Among other roles, PI3Ks regulate phagocytosis by driving re-arrangement of actin in phagosome formation[38,39]. Class 1A PI3Ks – the p110α, p110β and p110δ isoforms -- positively regulate the small G protein Rac1[40], which coordinates actin organization and is required for FcR-mediated phagocytosis[41,42]. Of these, the p110δ isoform has also been shown to selectively reduce phosphorylation of Akt which is an upstream effector of FcR-mediated phagocytosis[43] and negatively regulate the PI3K antagonist, PTEN, in murine macrophages[44]. To test whether PI3Kδ inhibition would attenuate the forces generated in FcR-mediated phagocytosis, we subjected hMDMs contracting our hIgG micropatterns to three steps of 10-fold dilutions of the selective p110δ inhibitor, CAL-101.

We found that at the effective dose (ED) of 1 μM, compared to the vehicle control, CAL-101 produced statistically significant relaxations in micropatterns occupied by the active population of macrophages and at 10 μM the effect was even more pronounced indicating a dose-dependent response (Fig. 6A–D). Although pre-treatment with CAL-101 produced a more robust relaxation at all doses, the post-contraction incubation revealed the rapid onset of this effect (which became noticeable within 15 min of compound addition), and corroborated the requirement of PI3K activity for sustained force generation. This observation shows for the first time that PI3K plays a direct role in phagocytic force generation. The partial suppression of baseline phagocytic force at the ED is consistent with reports that PI3K inhibition blocks phagocytosis of large targets but not smaller ones[38]. It is also possible that the redundant functions of the other class 1A PI3Ks helped to mitigate the relaxing effects of this selective p110δ inhibition. This observation is important to consider in terms of potential immunosuppresive side-effects of CAL-101 which is currently in Phase 3 clinical trials for treatment of chronic lymphocytic leukemia (Clinical Trials Identifier NCT01539291).

Discussion

The FLECS system combines breakthroughs in the preparation of bio-functionalization of soft materials with compatibility with automation workflows to enable high-throughput and multi-modal analysis of large populations of a variety of contractile cells. The core material allows for independently tunable stiffness, pattern shape, and molecular composition, allowing it to be tailored to a broad range of cell types and their functions, while the seamless integration with well-plate formats enables direct use with screening robotics and high-content imagers, as well as simple adoption by end-users. As such this system has the potential to address both unique research and industrial applications.

For example, the functionalization of our sensors with immunological molecules enables the study of phagocytosis of large targets. Whereas traditional phagocytosis assays are endpoint measurements that look at the total engulfment by phagocytes of exclusively smaller targets, our larger surface-bound targets are a good model for phagocytosis of tissue-like structures such as biofilms or tumor cells embedded in tissue. In addition to quantifying phagocytic force, this method could help determine which factors can lead to improved immune cell disruption of such pathogenic tissue-like structures. By simply altering surface functionalization, evaluations of forces by many other cell types, including smooth muscle cells or cardiomyocytes (Fig. S8, Movies S8–S10) also become possible.

The FLECS system's compatibility with automation enables precise execution of multi-parametric studies of large quantities of different cells. We were able to simultaneously evaluate tone, responsiveness to an agonist, and subsequent responsiveness to a countering antagonist, for >1000 of cells from each of 12 patient-derived cell lines at once using a single FLECS well-plate. The overall yield of ~31,000 cells on the plate, of which ~ 24,000 were robust responders and used for analysis, exceeds previously reported throughputs for individual contractility experiments (which we define as comprising a single cell-seeding session and single execution of analysis software) by 100-fold. Through analyzing this many cells simultaneously, we were able to definitely report that asthma HASM innately produce larger forces than non-asthma HASM.

Although we observed clear differences between multipotent and differentiated cells, the differences between osteocytes and adipocytes were less apparent, despite past reports showing such differences using micropost arrays[22]. Whether this discrepancy is a result of the fundamentally different physical environments presented to the cells (continuous planar vs. discretized deflectable pillars), different culture conditions (*in situ* vs *in vitro*) or due to resolution limitations is unclear. Therefore, it is important to note that each of the three major laboratory methods for measuring cellular force offer unique strengths and limitations, and a given biological problem may be better suited by one method over another. These are summarized in Table 1 and discussed below.

As discussed, TFM and micropost array methods still offer superior spatial resolution that is able to assign force vectors to specific focal adhesions, and to measure very subtle forces in small cells like T-cells. Advanced TFM techniques are now able to map complex subcellular forces in three-dimensional polymer and gel networks. In general, both methods should remain the standard for addressing specific biological questions relating to sub-cellular force-generation by small numbers of cells. However, this resolution comes at the cost of simplicity and throughput, as these methods typically require high magnification imaging and manual user input during analysis workflows. Thus, as shown in Table 1, the experimental data throughputs have generally been limited to 10–50 cells.

In comparison, FLECS is demonstrated to yield a larger quantity of single-cell data per experiment than the older methods. Instead of manually tracing, or fixing and staining cells (which may alter the observable contractile phenotype substantially), FLECS analysis locates live cells based on nuclear staining co-localized to micro-pattern sites using automated template-matching and binary segmentation algorithms. Thus, no user input is

required and all imaged cells are analyzed, thereby removing the potential for selection bias. Furthermore, by taking whole-cell rather than sub-cellular force measurements, FLECS is able to extract quantitative data from much larger fields-of-view with smaller pixel sizes (e.g. data presented in Fig. 3 and Fig. 4 was extracted from images taken with 1.61 μm/px sizes) relative to the older methods. Finally, as discussed at length, FLECS is the only platform demonstrated to integrate into a high-throughput phenotypic screening configuration that maintains *single-cell resolution*. These features enable FLECS to achieve the described 100-fold improvements in throughput.

All three methods are suitable for performing time-course measurements of cellular force. However, in addition to throughput limitations, unconstrained cells in the native TFM and micropost systems will migrate and require precise monitoring, adding a layer of complexity to the measurements. This problem can be overcome by incorporating microcontact printing steps to restrict cell motion, although this may present additional fabrication difficulties. With FLECS, cells are inherently restricted to micropatterns and do not migrate. For the same reason, FLECS inherently provides single-cell resolution which allowed us to longitudinally track cellular contractility following calcium imaging in the same single cells to discover that peak measurements in these two modes are not well correlated despite calcium flux being commonly used as a direct upstream indicator, as well as to select for responding cells from both HASM and macrophage populations to cleanly resolve agonist effects.

As a result of these unique advantages FLECS has the potential to become the leading technology for phenotypic drug discovery pertaining to conditions involving aberrant cellular force-generation. Compared to target-based screening, phenotypic screening has produced more first-in-class medicines due to its naturally unbiased identification of molecular mechanism of action[57].

Methods

Preparation of patterned ultra-soft substrates

The wafer-scale process is shown in Fig. S9 and has been described in detail previously[58]. Briefly, a 20% dextran solution (70 kDa from Sigma Aldrich) in deionized water was spin-coated onto plasma-activated silicon wafers and baked until dehydration to yield dextran substrates. Chrome photomasks containing arrays of micro-patterns were designed using L-Edit software, fabricated off-site, and used to pattern SPR 220 photoresist on separate silicon wafers. PDMS (Sylgard 184) at 10:1 ratio of base:crosslinker was cast onto the patterned wafer, cross-linked and demolded yielding stamps with positive pattern features. Adhesive biomolecule (e.g. ECM protein) solution was added to the stamp surface, incubated for 1 hr, and air-dried immediately before stamping. The stamped adhesive molecule or a co-stamped molecule was conjugated with a fluorescent moiety. Dextran substrates were activated with a brief plasma treatment and stamped with the biomolecule-adsorbed PDMS stamps for 5 minutes. Ultra-soft PDMS mixture (55:1 to 71:1) was spin-coated (1200 rpm, 20 s) over the stamped dextran-coated silicon, and cured (24 hrs RT followed by 7 days at 65 °C). Once cured, the substrate may be stored stably at room temperature for >9 months.

Releasing substrates and seeding with cells

To begin an experiment, the substrate is mounted onto cover glass (where the PDMS layer is in contact with the cover glass) and placed into saline solution to release the soluble dextran layer and yield a glass-backed elastomeric thin-film with embedded proteins. This substrate may be fabricated as large as a well-plate footprint. Following fabrication, the sample is sterilized by washes in strong base followed by washes in sterile deionized water. Non-patterned regions are blocked in a 0.5% solution of Pluronics F-127 (45 mins, RT) and cells of interest are seeded. For live imaging experiments, Hoechst 33342 nuclear stain is added to the culture medium (1 μg mL^{-1} final concentration). If cells are to be fixed, the nucleus is stained after fixation. The sample is washed to remove non-adhered cells after 2 hr. At the conclusion of the experiment, the sample is either left unfixed or fixed in 4% paraformaldehyde solution at RT for 1 hr and mounted using DAPI-infused mounting medium, and imaged.

Imaging and image analysis

In our experiments, fluorescent patterns (green or red channel) and cell nuclei (blue channel) were imaged at 10X magnification with a Nikon fluorescent microscope in fixed-sample experiments, or with the ImageXpress® Micro XL High-Content Imaging System fluorescent microscope with 10X magnification for end-point experiments, or 4X for time-course experiments. Image processing was performed with MATLAB.

A separate algorithm was developed for analyzing each pattern type. For experiments using cross ('X') patterns, a template is used to locate all patterns in all frames. The mean distance between the center and each terminal of each pattern comprises a data point. For experiments using circular patterns, the native MATLAB function *imfindcircles()* is used to identify all circular shapes in each frame and measure their radii. The presence or absence of a stained nucleus at the corresponding *xy* location of the nuclear image determines whether a given pattern is used for the control data, experimental data, or is rejected as having multiple cells (Fig. S2A). All experimental data measurements were zeroed to the median of the measurements of control case patterns yielding net displacement histogram plots. Raw measurements are also saved in a *.mat* format.

During processing, a file containing (i) an image of each cross pattern marked at the computed center and vertices, or an image of each circular pattern overlaid with the circle fitted by the *imfindcircles()* function, alongside (ii) an image of the corresponding nuclear signal labeled with the computed cell count, is created and saved for each pattern-nuclear signal pair for later viewing and quality control (Fig. S2B).

Study on mesenchymal stem cells

Cell Culture and Differentiation.—Human mesenchymal stem cells (hMSCs) derived from bone marrow or adipose tissue (StemPro) were maintained in MesenPRO RS™ Medium. Differentiation was induced by 14 day culture in adipogenic (StemPro Adipogenesis Differentiation Kit) or osteogenic (StemPro Osteogenesis Differentiation Kit) inductive medium as described in the manufacturer's manual. Trypsin-EDTA (.05%) was used to resuspend cells at the start of the experiment. Seeding and culturing on FLECS

substrates was done in Dulbecco's modified Eagle medium (DMEM, Invitrogen) supplemented with 10% MSC Qualified FBS, 100 units mL^{-1} penicillin and 100 μg mL^{-1} streptomycin. Early passages (<7) of hMSCs were used in all experiments.

Substrate Parameters.—Cross shaped patterns (70 μm diagonal, 10 μm bar thickness) spaced at 100 μm center-to-center vertical and horizontal distances were used for this experiment. Substrates we prepared by adsorbing 0.5 mL of 30 μg mL^{-1} fibronectin and 30 μg mL^{-1} Alexa Fluor 488-conjugated fibrinogen solution to each of six 22mm × 22mm stamps for 45 mins before stamping dextran-coated wafers. PDMS was mixed at a 55:1 base to crosslinker ratio.

Experimental Procedure.—Substrates were housed in 6-well plates during the experiment. Cells were seeded by pipetting cell suspensions directly over the substrates. After 1hr, non-adhered cells were washed away. Cells were fixed with warmed 4% paraformaldehyde and the substrates were mounted onto glass slides using DAPI-infused mounting medium (ThermoFisher P-36931) 8 hours after seeding and later imaged.

Actin Staining.—Following fixation and prior to mounting, a subset of all MSC samples were permeabilized with 0.25% Triton X-100 (Sigma) for 10 mins and incubated with 1:500 Alexa fluor-568 phalloidin (ThermoFisher, A12380) in PBS for 20 minutes at RT.

Study on tonic traction forces supplied by primary human smooth muscle cells

Cell culture.—Cryopreserved human primary bronchial, uterine, and aortic smooth muscle cells were purchased from Promocell. The cells were maintained in complete Smooth Muscle Medium (Promocell) supplemented with 100 units mL^{-1} penicillin and 100 μg mL^{-1} streptomycin. Trypsin-EDTA (.05%) was used to re-suspend cells at the start of the experiment. Seeding and culturing on FLECS substrate was also done in Complete SMC 2 Medium (Promocell). An end-point measurement was obtained from one well for each SMC source at 8 hours after seeding.

Blebbistatin titration

Blebbistatin (Sigma Aldrich) was dissolved in DMSO to achieve working concentrations using 10 steps of 2-fold dilutions beginning with 25 μM. HASM cells were seeded 24 hrs prior to treatment with blebbistatin. On the day of the experiment, cells were stained with Hoechst, washed, treated with blebbistatin (1% DMSO final concentration), incubated for 30 mins and imaged live using the ImageXPress Micro XL High Content Imaging System.

Statistical Analysis.—Each concentration of blebbistatin was tested in 4 technical replicates. Median contraction at each concentration was normalized by vehicle-treated contraction. GraphPad Prism 6 graphing software was used to fit a sigmoid curve to the dose-response data and calculate the half maximal inhibitory concentration.

Evaluation of asthma and non-asthma patient-derived HASM

Isolation and culture of HASM.—All lines of HASM cells were derived from tracheas obtained from the National Disease Research Interchange (Philadelphia, PA, USA) and from

the International Institute for the Advancement of Medicine (Edison, NJ, USA). HASM cell culture was performed as described previously[59–61]. Briefly the cells were cultured in Ham's F- 12 medium supplemented with 10% FBS, 100 U mL- 1 penicillin, 0.1 mg mL- 1 streptomycin and 2.5 mg mL- 1 amphotericin B, and this medium was replaced every 72 h. HASM cells passages 1–6 were used for all experiments, because these cells retain the expression of native contractile protein, as demonstrated by immunocytochemical staining for smooth muscle actin and myosin[59]. The HASM cells were derived from donors with fatal asthma or from donors who were age- and gender- matched without asthma as shown in Table S1.

The 12 distinct patient cell lines were seeding into 8 wells, column-by-column alternating between non-asthmatic and asthmatic lines, in each of 3 FLECS well-plates at approx. 5000 cells per well and allowed to adhere for 2 hours, at which points serum was removed for 24 hours before pro-contractile agonists were added.

Basal Tone.—The three plates were imaged on an ImageXpress high-content imager with environmental controls prior to any stimulation to get a basal measurement for contraction.

Responsiveness to bradykinin and formoterol.—Immediately after acquiring baseline images, one of the three well-plates (selected at random) was used to perform pharmacological studies, and a multi-drop instrument (BioTek) was used to deliver bradykinin (Sigma) to all 96 wells at a final concentration of 10 μM. The plate was replaced on the imager and each well was imaged for 16 mins at 4 min intervals. Following the last imaging time-point, the plate was removed and the multi-drop was used to deliver 50 μM fomroterol (Sigma) to every odd row, or 1% DMSO in serum-free medium to every even row. The plate was again replaced and imaged an addition 6 time-points. Analysis software was used to track contractile behavior of each of the 250–450 cells adhered within each well (>31,000 cells total) over the course of the experiment, and those cells exhibiting a positive contraction between the initial time-point and 4th time-point (after 16 minutes of bradykinin stimulation but prior to formoterol or vehicle) were selected for further analysis – approximately 24,000 cells.

Simultaneous measurements of calcium release and contractility in HASM single-cells

Experimental.—HASM cells derived from a single healthy patient were seeded into a FLECS well-plate as described above and serum-starved for 24 hours. Prior to imaging, cells were incubated with 4 μM Fluo-8 (Abcam) and 1 μg mL^{-} Hoechst 33342 for 1 hr and then washed with fresh serum-free medium. To start the experiment, 20 wells were imaged using 4X magnification on the ImageXpress to get a baseline reading. The plate was immediately transported to a table-top manual fluorescent microscope (Nikon) where serum-free medium, 20% FBS (ThermoFisher), 10 μM bradykinin, 100 nM endothelin-1 (Sigma), or 10 μM histamine (Sigma) was added to 4 wells each, one-by-one, and the calcium dye intensity was imaged for 30s at 100ms intervals (see: Movie S6). After the imaging was complete for the final well, the plate was transported back to the high-content imager to acquire images of the micropatterns for 25 minutes at 1 minute intervals.

Analysis.—Image-series of the micropatterns and image-series of the calcium signal, which were acquired on separate microscopes, were registered using corresponding images of stained cell nuclei taken at both microscopes which produced a unique intensity signature at each site allowing simple registration in ImageJ. Single-cell contraction was assessed as usual. Micropatterns in the images taken at the initial time-point were used to define regions of interest for each cell within which calcium dye intensity was calculated for every frame and normalized to initial intensity. In the case of 20% serum, addition generated significant sustained auto-fluorescence so the authors manually adjusted the reference intensity for those wells as it was clear from the traces when the calcium peaked relative to addition of serum. The other agonist did not produce a sustained auto-fluorescence. Both the calcium release and contractility traces were pooled and averaged to generate mean traces shown in Fig. 4C. The initial calcium peaks were used to register all calcium traces prior to averaging. The peak values obtained from each single-cell contractility and calcium trace were also displayed in a scatter plot to generate Fig. 4D.

Phagocyte experiments

Macrophage Differentiation.—Human peripheral blood monocytes were isolated from blood taken from consenting healthy adult donors using density gradient centrifugation with Histopaque®−1077 solution (Sigma) according to UCLA IRB protocol #14–000522. Collected mononuclear cells were washed in saline, resuspended in unsupplemented RPMI 1640 medium (Life Technologies) and allowed to adhere to the well surfaces within polystyrene 6-well-plates for 2 hrs. The wells were then washed to remove contaminating lymphocytes and refilled with warm RPMI 1640 medium supplemented with 20% heat inactivated FCS, 20 ng mL^{-1} M-CSF (Life Technologies), 100 units mL^{-1} penicillin and 100 μg mL^{-1} streptomycin. Monocytes were allowed to differentiate into macrophages (hMDM) for 7 days. All macrophages were used within this period as phagocytic force was significantly reduced in macrophages aged >14 days and completely suppressed in macrophages aged 21 days **(**Fig. S10). To begin an experiment, macrophages were dissociated from the well-plates by incubation in StemPro® Accutase® (Life Technologies) for 30 mins at 37°C, followed by vigorous pipetting up and down to complete dissociation. Macrophages were resuspended in RPMI 1640 medium supplemented with 10% heat inactivated FCS, 100 units mL^{-1} penicillin and 100 μg mL^{-1} streptomycin before seeding onto FLECS chips. Macrophages were imaged live without fixing in all experiments and Hoechst 33342 (1 μg mL^{-1}) was used to stain cell nuclei.

Dendritic Cell Differentiation.—Dendritic cells were prepared in the same manner as macrophages but using differentiation medium containing 100ng/mL GM-CSF and 50 ng/mL IL-4 instead of M-CSF.

Patterning Antibodies.—To pattern IgG antibodies, a 45 μg mL^{-1} dansyl-conjugated bovine serum albumin and 45 μg mL^{-1} Alexa Fluor 488-conjugated bovine serum albumin solution was adsorbed to a stamp and stamped onto a dextran-coated wafer. After the substrates were coated with PDMS, cured, released and blocked with Pluronic F127 but before seeding macrophages, approximately 50 μL per 400 mm^2 of 25 μg mL^{-1} solution of human-mouse chimeric anti-dansyl IgG antibodies was spread over each patterned substrate

and incubated for 3 hrs at RT. Excess antibody was then washed with saline. The human-mouse chimeric antibodies were developed by Morrison *et al*[62].

Density-Dependence Experiment.—Circular patterns with 54 μm diameters but with various degrees of filling were patterned with IgG as described above. Specifically, (i) a ring pattern with 10 μm thickness (inner diameter subtracted from the outer diameter), (ii) the same ring pattern encircling a symmetric cross shape with 10 μm bar thickness and (iii) a solid circle were patterned. PDMS was mixed at a 65:1 base to crosslinker ratio. Macrophages were imaged 6 hours after seeding.

Opsonin-Dependence Experiment.—Human recombinant vitronectin (Advanced Biomatrix), fibrinogen (Life Technologies), BSA (Life Technologies) both conjugated with Alexa Fluor 488, and hIgG (as described above) were patterned in cross shapes (50 μm diagonal and 20 μm bar thickness). The total quantities of each ligand were set to be approximately uniform by modulating the concentrations of the adsorbing ligands and confirmed by measuring fluorescent intensities of resulting transferred patterns (Table S2). Macrophages were dissociated as described, seeded, and imaged live 6 hours later. PDMS was mixed at both 67:1 and 71:1 base to crosslinker ratios.

Patterning equal quantities of different opsonins.—Testing the phagocytic force response of hMDMs as a function of opsonin type required patterning of 3 different ligands: vitronectin, fibrinogen, dansyl-BSA, (hIgG was not patterned but rather used to bind the dansyl-BSA in which the conjugated dansyl group served as the binding site for the IgG antibodies). To decouple the potential effects of differential opsonin quantities from opsonin type, we set out to equalize the molar quantities of each opsonin on our substrates. To accomplish this, each opsonin was labeled with the same fluorophore (Alexa Fluor 488) and the respective degree of labeling (DOL) along with the fluorescent intensities of the patterns, as a function of solution concentration (used in the adsorption step), were used to achieve the same final surface densities. For each fluorescence intensity measurement, 10X magnification and 2 s exposure times were used.

Fibrinogen.—Alexa Fluor 488-conjugated fibrinogen was purchased from Life Technologies (Catalog #F13191, Lot #1636855) with a DOL of 6. This was the same ligand as was used for the hMSC and dose-response experiments and was adsorbed to the PDMS stamps for 45 mins before being stamped onto the dextran-coated wafers for 5 mins. Three concentrations (30, 20 and 10 μg mL-1) were tested to create a concentration vs. fluorescent intensity curve.

BSA.—Alexa Fluor 488-conjugated BSA was purchased from Life Technologies (Catalog #A13100, Lot #1348652) with a DOL of 7. Alexa Fluor 488-conjugated BSA (AF488-BSA) was co-patterned with dansyl-BSA since the former was used for fluorescently visualizing the pattern while the latter contained the epitope (dansyl) targeted by our human-mouse chimeric antibody. Thus, the two BSA molecules were patterned in equal quantities at three concentrations (60, 30 and 20 μg mL-1 each) to create a concentration vs. fluorescent intensity curve. In addition to the general procedure, the PDMS stamps were plasma treated

before adsorption to promote wetting and during stamping, the stamps were kept in contact with the dextran-coated wafers under weight for 20 min rather than 5 min.

HIgG.—BSA patterns were prepared as described with the addition of hIgG (50 μL of 25 μg mL^{-1} solution per 400 mm^2) after the release, sterilization and blocking steps.

Vitronectin.—Human recombinant vitronectin was purchased from Advanced Biomatrix (Catalog #5052) and conjugated with Alexa Fluor 488 in-house using Alexa Fluor 488 carboxylic acid, succinimidyl ester (Life Technologies) at a 8:1 fluorophore to protein molar ratio in PBS (4 hrs, 4C). Following the reaction, the vitronectin solution was dialyzed against PBS for 48 hours with PBS changes every 12 hours to remove unreacted dye. The DOL for the vitronectin-Alexa Fluor 568 conjugate was calculated to be 6.25 using absorbance readings taken at 494 and 280 nm, as prescribed in the manufacturer's manual provided with the conjugation kit from Life Technologies, and using 1.02.mL mg^{-1} cm^{-1} as the extinction coefficient for vitronectin[63]. Three concentrations (40, 30 and 20 μg mL^{-1}) were tested to create a concentration vs. fluorescent intensity curve. Like with BSA, the stamps were plasma-treated before adsorption and the stamps were kept in contact with the dextran-coated wafers under weight for 20 mins.

BSA.—BSA was found to saturate in fluorescent intensity when 30 μg mL^{-1} and higher concentrations were used for each BSA conjugate. However, concentrations of 60 μg mL^{-1} produced the most consistent transfers so this concentration was chosen for BSA. This maximum BSA intensity was normalized by the DOL for BSA and adjusted by a factor of 2 to account for the equal part of non-fluorescent BSA (dansyl-BSA). Referencing this target normalized intensity (termed the 'relative surface molarity coefficient'), along with the concentration vs. fluorescent intensity curves constructed for vitronectin and fibrinogen and their DOLs, we predicted the adequate concentrations to be 30 μg mL^{-1} and 10 μg mL^{-1} for vitronectin and fibrinogen, respectively.

Approximation of phagocytic forces

Substrate stiffness measurement.—Cylindrical PDMS samples (67:1 and 71:1) were placed onto an Instron tensile tester (Model 5564, Norwood, MA) with a 2.5 N load cell and compressive testing of the sample was performed at strain rate of 1 mm/min for a total indentation of 1.5 mm. The data was used to generate load-displacement curves. The slope of the linear portion of the curve, the cross-sectional area of the indentation tip and the PDMS sample heights were used to calculate stiffness. Three samples of each stiffness were test after 1 week and after 3 weeks of curing (Fig. S11). The results showed no significant stiffening after 1 week indicating the polymer was fully cured at one week and these unchanging stiffness values could be used for modeling cellular traction forces. The mean calculated stiffnesses were used in force approximations.

Finite element method modeling.—To approximate forces applied by phagocytosing macrophages on the ultra-soft substrates, the FLECS 'X' pattern was simulated using finite element model software, COMSOL (COMSOL, Inc.). Specifically, a single cross-shaped pattern corresponding to the experimental patterns (50 μm diagonal, 10 μm bar thickness)

was simulated. We modeled the ultra-soft substrates as linear elastic materials with Young's moduli: 4000 Pa, 7900 Pa (corresponding to 71:1 and 67:1 PDMS ratios, respectively) density: 970 kg/m^3, Poisson's ratio: .49999, and the forces exerted by macrophages as boundary loads directed tangentially between all pairs of adjacent terminals of the 'X' pattern. The substrate was modeled as a 150 μm by 150 μm film with thickness of 90 μm and was discretized into tetrahedral mesh elements. A 90 μm thickness was selected to minimize computational intensity associated with higher degrees of freedom, as thicknesses greater than 70 μm did not yield significant changes in pattern deflection for a given applied force. (Empirically, substrates were determined to be approximately 110 μm thick by using an automated fluorescent microscope to find the two focal planes containing either the embedded patterns or the glass substrate and calculating the distance between them). The bottom of the modeled substrate was assigned a fixed boundary condition (displacement = 0) and tangential forces ranging from 1 nN to 250 nN were applied to 5 μm by 10 μm regions on the top surface of the modeled substrate at the vertices of the pattern. In order to compute the pattern displacement due to an applied force, max values of the in-plane deformation were calculated on the four edges of the pattern region. Due to symmetry, the points of maximum displacement were located at the centerpoints of each terminal boundary, which is the same location the imaging analysis algorithm measures displacement.

For this model, the key assumptions of elasticity and linearity hold. Relaxation of contracted cells with the myosin inhibitor blebbistatin results in patterns returning to their unperturbed size and shape, suggesting elastic behavior and a lack of plastic deformation (Movie S3). Additionally, previous work has demonstrated that PDMS behaves as a linearly elastic material under quasi-static loading conditions[64]. Finally, the observed deflections of the substrate are small in comparison to the size of the substrate so we do not expect significant departures from linearity. This model is similar to that employed by Oakes PW, *et al.*[14], though our system allows for direct measurement of substrate deflection, removing the need for including the cell in the simulation.

Macrophage drug panel

Experimental.—Cell culture and substrate preparation was identical to our earlier macrophage experiments, but using exclusively hIgG patterns. Chloroquine, CAL-101, and cytochalasin D were dissolved in medium or DMSO and delivered to FLECS-plate wells at final concentrations of 0.1, 1 and 10 μM either before macrophages were seeded, or after macrophages had maintained adhesion to the patterns for 24 hours. In the former case, imaging was done 24 hours later. In the latter, imaging was done 15 minutes after addition of the drug.

Analysis.—Since an inactive subpopulation of macrophages was prevalent in the overall population, we fitted a mixed Gaussian curve to each distribution using the open-source MATLAB function *peakfit.m* developed by Prof. Tom O'Haver from the University of Maryland. For obtaining the best fit, the two Gaussian widths were restricted to a minimum of 1 but were otherwise unconstrained. In each case (except with pre-treatment with cytochalasin D), two Gaussians were clearly identified in the best fit representing the inactive (near-zero contraction) and active populations. Overall curve fit error rates were low

at <7% and R-squared values were all > 0.93. The central positions of the Gaussian's representing the active populations were used for quantifying the contractile capability of the macrophages following treatment with vehicle or drug.

Cardiac myocyte experiments

Cell culture and imaging.—Freshly isolated neonatal rat ventricular myocytes were a generous gift from Josh Zixi Lee and Prof. Yibin Wang. Immediately after isolation, the cells were brought in suspension in DMEM media supplemented with 1% Insulin-transferrin-sodium selenite, and seeded onto samples patterned either with fibronectin-fibrinogen cross-shaped patterns (50 μm diagonal, 10 μm thickness) or 200 μm^2 rod shaped patterns with a 7:1 length ratio. Approximately 6 hrs after seeding, spontaneous beating was observed in a fraction of cells. Patterns contracted by beating cells were imaged using fast time-lapsed imaging with short exposure times (e.g. 100 ms) enabling real time observations of the contractions.

Electrical stimulation.—To pace the cells, an assembly was created based on previous work[65]. Briefly, carbon rods were placed in parallel 5 cm in a petri dish and held in place using cured Sylgard 184. Platinum wire was wrapped around each carbon rode and connected to either electrode on a Grass Intrument SD9 pulse generator. Pulse widths of 10 μs and 80V were applied at 1 or 2 Hz to pace cardiac cells adhered to patterns placed inside the petri dish.

Supplementary Material

Refer to Web version on PubMed Central for supplementary material.

Acknowledgements

The work was supported by the NIH Director's New Innovator Award # 1DP2OD007113, NIH 5R21EB024081 and David and Lucile Packard Fellowship. The authors would like thank Dr. Chris Walthers for providing primary mouse intestinal smooth muscle cells, Prof. Yibin Wang and Josh Zixi Lee for providing NRVMS, and Dr. Oladunni Adeyiga for performing bloods draws over the course of 6 months to facilitate primary macrophage culture. All microfabrication steps were completed using equipment provided by the Integrated Systems Nanofabrication Cleanroom (ISNC) at the California NanoSystems Institute (CNSI) at UCLA.

References

1. Discher DE, Janmey P & Wang Y-L Tissue cells feel and respond to the stiffness of their substrate. Science 310, 1139–1143 (2005). [PubMed: 16293750]
2. Fournier MF, Sauser R, Ambrosi D, Meister J-J & Verkhovsky AB Force transmission in migrating cells. J. Cell Biol 188, 287–297 (2010). [PubMed: 20100912]
3. Burton K & Taylor DL Traction forces of cytokinesis measured with optically modified elastic substrata. Nature 385, 450–454 (1997). [PubMed: 9009194]
4. Evans E, Leung A & Zhelev D Synchrony of cell spreading and contraction force as phagocytes engulf large pathogens. J. Cell Biol 122, 1295–1300 (1993). [PubMed: 8376464]
5. Hall CN et al. Capillary pericytes regulate cerebral blood flow in health and disease. Nature 508, 55–60 (2014). [PubMed: 24670647]
6. Pelaia G et al. Molecular mechanisms underlying airway smooth muscle contraction and proliferation: Implications for asthma. Respiratory Medicine 102, 1173–1181 (2008). [PubMed: 18579364]

7. Yemisci M et al. Pericyte contraction induced by oxidative-nitrative stress impairs capillary reflow despite successful opening of an occluded cerebral artery. Nat. Med 15, 1031–1037 (2009). [PubMed: 19718040]
8. Huang X et al. Relaxin Regulates Myofibroblast Contractility and Protects against Lung Fibrosis. Am J Pathol 179, 2751–2765 (2011). [PubMed: 21983071]
9. Valencia AMJ et al. Collective cancer cell invasion induced by coordinated contractile stresses. Oncotarget 6, 43438–43451 (2015). [PubMed: 26528856]
10. Gupta S, Nahas SJ & Peterlin BL Chemical Mediators of Migraine: Preclinical and Clinical Observations. Headache 51, 1029–1045 (2011). [PubMed: 21631491]
11. Munevar S, Wang Y & Dembo M Traction force microscopy of migrating normal and H-ras transformed 3T3 fibroblasts. Biophys J 80, 1744–1757 (2001). [PubMed: 11259288]
12. Park CY et al. High-throughput screening for modulators of cellular contractile force. Integr Biol (Camb) 7, 1318–1324 (2015). [PubMed: 25953078]
13. Tan JL et al. Cells lying on a bed of microneedles: An approach to isolate mechanical force. PNAS 100, 1484–1489 (2003). [PubMed: 12552122]
14. Oakes PW, Banerjee S, Marchetti MC & Gardel ML Geometry Regulates Traction Stresses in Adherent Cells. Biophys J 107, 825–833 (2014). [PubMed: 25140417]
15. Ricart BG, Yang MT, Hunter CA, Chen CS & Hammer DA Measuring Traction Forces of Motile Dendritic Cells on Micropost Arrays. Biophys J 101, 2620–2628 (2011). [PubMed: 22261049]
16. Legant WR et al. Multidimensional traction force microscopy reveals out-of-plane rotational moments about focal adhesions. PNAS 110, 881–886 (2013). [PubMed: 23277584]
17. Polacheck WJ & Chen CS Measuring cell-generated forces: a guide to the available tools. Nat Meth 13, 415–423 (2016).
18. Myers DR et al. Single-platelet nanomechanics measured by high-throughput cytometry. Nat Mater 16, 230–235 (2017). [PubMed: 27723740]
19. Tseng Q et al. A new micropatterning method of soft substrates reveals that different tumorigenic signals can promote or reduce cell contraction levels. Lab Chip 11, 2231–2240 (2011). [PubMed: 21523273]
20. Rape A, Guo W & Wang Y The Regulation of Traction Force in Relation to Cell Shape and Focal Adhesions. Biomaterials 32, 2043–2051 (2011). [PubMed: 21163521]
21. Wang N, Ostuni E, Whitesides GM & Ingber DE Micropatterning tractional forces in living cells. Cell Motil. Cytoskeleton 52, 97–106 (2002). [PubMed: 12112152]
22. Fu J et al. Mechanical regulation of cell function with geometrically modulated elastomeric substrates. Nat Meth 7, 733–736 (2010).
23. Kim HR, Appel S, Vetterkind S, Gangopadhyay SS & Morgan KG Smooth muscle signalling pathways in health and disease. J Cell Mol Med 12, 2165–2180 (2008). [PubMed: 19120701]
24. Limouze J, Straight AF, Mitchison T & Sellers JR Specificity of blebbistatin, an inhibitor of myosin II. J Muscle Res Cell Motil 25, 337–341 [PubMed: 15548862]
25. Straight AF et al. Dissecting Temporal and Spatial Control of Cytokinesis with a Myosin II Inhibitor. Science 299, 1743–1747 (2003). [PubMed: 12637748]
26. An SS et al. An inflammation-independent contraction mechanophenotype of airway smooth muscle in asthma. J. Allergy Clin. Immunol 138, 294–297.e4 (2016). [PubMed: 26936804]
27. Herington JL et al. High-Throughput Screening of Myometrial Calcium-Mobilization to Identify Modulators of Uterine Contractility. PLOS ONE 10, e0143243 (2015). [PubMed: 26600013]
28. Wertek F & Xu C Digital response in T cells: to be or not to be. Cell Res 24, 265–266 (2014). [PubMed: 24407423]
29. McNally AK, Jones JA, Macewan SR, Colton E & Anderson JM Vitronectin is a critical protein adhesion substrate for IL-4-induced foreign body giant cell formation. J Biomed Mater Res A 86, 535–543 (2008). [PubMed: 17994558]
30. Labernadie A, Thibault C, Vieu C, Maridonneau-Parini I & Charrière GM Dynamics of podosome stiffness revealed by atomic force microscopy. Proc. Natl. Acad. Sci. U.S.A 107, 21016–21021 (2010). [PubMed: 21081699]

31. Gordon S & Taylor PR Monocyte and macrophage heterogeneity. Nat. Rev. Immunol 5, 953–964 (2005). [PubMed: 16322748]
32. Soon CF, Tee KS, Youseffi M & Denyer MCT Tracking Traction Force Changes of Single Cells on the Liquid Crystal Surface. Biosensors (Basel) 5, 13–24 (2015). [PubMed: 25808839]
33. Tsang PH, Li G, Brun YV, Freund LB & Tang JX Adhesion of single bacterial cells in the micronewton range. PNAS 103, 5764–5768 (2006). [PubMed: 16585522]
34. Hind LE, Dembo M & Hammer DA Macrophage Motility is Driven by Frontal-Towing with a Force Magnitude Dependent on Substrate Stiffness. Integr Biol (Camb) 7, 447–453 (2015). [PubMed: 25768202]
35. Goh YS et al. Human IgG isotypes and activating Fcγ receptors in the interaction of Salmonella enterica serovar Typhimurium with phagocytic cells. Immunology 133, 74–83 (2011). [PubMed: 21323662]
36. Kaplan G Differences in the Mode of Phagocytosis with Fc and C3 Receptors in Macrophages. Scandinavian Journal of Immunology 6, 797–807 (1977). [PubMed: 561436]
37. Hackam DJ, Rotstein OD & Grinstein S Phagosomal acidification mechanisms and functional significance in Advances in Cellular and Molecular Biology of Membranes and Organelles (ed. Gordon S) 5, 299–319 (JAI, 1999).
38. Schlam D et al. Phosphoinositide 3-kinase enables phagocytosis of large particles by terminating actin assembly through Rac/Cdc42 GTPase-activating proteins. Nat Commun 6, 8623 (2015). [PubMed: 26465210]
39. Beemiller P et al. A Cdc42 Activation Cycle Coordinated by PI 3-Kinase during Fc Receptor-mediated Phagocytosis. Mol Biol Cell 21, 470–480 (2010). [PubMed: 19955216]
40. Papakonstanti EA et al. Distinct roles of class IA PI3K isoforms in primary and immortalised macrophages. J. Cell. Sci 121, 4124–4133 (2008). [PubMed: 19033389]
41. Castellano F, Montcourrier P & Chavrier P Membrane recruitment of Rac1 triggers phagocytosis. J Cell Sci 113, 2955–2961 (2000). [PubMed: 10934035]
42. Massol P, Montcourrier P, Guillemot J-C & Chavrier P Fc receptor-mediated phagocytosis requires CDC42 and Rac1. The EMBO Journal 17, 6219–6229 (1998). [PubMed: 9799231]
43. Ganesan LP et al. The Serine/Threonine Kinase Akt Promotes Fcγ Receptor-mediated Phagocytosis in Murine Macrophages through the Activation of p70S6 Kinase. J. Biol. Chem 279, 54416–54425 (2004). [PubMed: 15485887]
44. Papakonstanti EA, Ridley AJ & Vanhaesebroeck B The p110δ isoform of PI 3-kinase negatively controls RhoA and PTEN. EMBO J 26, 3050–3061 (2007). [PubMed: 17581634]
45. Beussman KM et al. Micropost arrays for measuring stem cell-derived cardiomyocyte contractility. Methods 94, 43–50 (2016). [PubMed: 26344757]
46. Cheng Q, Sun Z, Meininger G & Almasri M PDMS elastic micropost arrays for studying vascular smooth muscle cells. Sensors and Actuators B: Chemical 188, 1055–1063 (2013).
47. Munevar S, Wang Y & Dembo M Traction Force Microscopy of Migrating Normal and H-ras Transformed 3T3 Fibroblasts. Biophysical Journal 80, 1744–1757 (2001). [PubMed: 11259288]
48. Wu H et al. Epigenetic Regulation of Phosphodiesterases 2A and 3A Underlies Compromised β-Adrenergic Signaling in an iPSC Model of Dilated Cardiomyopathy. Cell Stem Cell 17, 89–100 (2015). [PubMed: 26095046]
49. del Álamo JC et al. Three-Dimensional Quantification of Cellular Traction Forces and Mechanosensing of Thin Substrata by Fourier Traction Force Microscopy. PLOS ONE 8, e69850 (2013). [PubMed: 24023712]
50. Plotnikov SV, Pasapera AM, Sabass B & Waterman CM Force fluctuations within focal adhesions mediate ECM-rigidity sensing to guide directed cell migration. Cell 151, 1513–1527 (2012). [PubMed: 23260139]
51. Goedecke N, Bollhalder M, Bernet R, Silvan U & Snedeker J Easy and Accurate Mechano-profiling on Micropost Arrays. J Vis Exp (2015). doi:10.3791/53350
52. Tolić-Nørrelykke IM & Wang N Traction in smooth muscle cells varies with cell spreading. Journal of Biomechanics 38, 1405–1412 (2005). [PubMed: 15922751]

53. Liu K et al. Improved-Throughput Traction Microscopy Based on Fluorescence Micropattern for Manual Microscopy. PLOS ONE 8, e70122 (2013). [PubMed: 23936383]
54. Colin-York H et al. Super-Resolved Traction Force Microscopy (STFM). Nano Lett. 16, 2633–2638 (2016). [PubMed: 26923775]
55. Murrell M, Oakes PW, Lenz M & Gardel ML Forcing cells into shape: the mechanics of actomyosin contractility. Nature Reviews Molecular Cell Biology 16, 486–498 (2015). [PubMed: 26130009]
56. Basu R et al. Cytotoxic T Cells Use Mechanical Force to Potentiate Target Cell Killing. Cell 165, 100–110 (2016). [PubMed: 26924577]
57. Swinney DC Phenotypic vs. target-based drug discovery for first-in-class medicines. Clin Pharmacol Ther 93, 299–301 (2013). [PubMed: 23511784]
58. Tseng P, Pushkarsky I & Carlo DD Metallization and Biopatterning on Ultra-Flexible Substrates via Dextran Sacrificial Layers. PLOS ONE 9, e106091 (2014). [PubMed: 25153326]
59. Panettieri RA, Murray RK, DePalo LR, Yadvish PA & Kotlikoff MI A human airway smooth muscle cell line that retains physiological responsiveness. Am. J. Physiol 256, C329–335 (1989). [PubMed: 2645779]
60. Koziol-White CJ et al. Inhibition of PI3K promotes dilation of human small airways in a rho kinase- dependent manner. Br. J. Pharmacol (2016). doi:10.1111/bph.13542
61. Yoo EJ et al. Gα12 Facilitates Carbachol-Induced Shortening in Human Airway Smooth Muscle By Modulating Phosphoinositide 3-Kinase-Mediated Activation In A RhoA-Dependent Manner. Br. J. Pharmacol (2017). doi:10.1111/bph.14040
62. Morrison SL, Johnson MJ, Herzenberg LA & Oi VT Chimeric human antibody molecules: mouse antigen-binding domains with human constant region domains. PNAS 81, 6851–6855 (1984). [PubMed: 6436822]
63. Zhuang P et al. Characterization of the Denaturation and Renaturation of Human Plasma Vitronectin II. INVESTIGATION INTO THE MECHANISM OF FORMATION OF MULTIMERS. J. Biol. Chem 271, 14333–14343 (1996). [PubMed: 8663085]
64. Vanlandingham MR, Chang N-K, Drzal PL, White CC & Chang S-H Viscoelastic characterization of polymers using instrumented indentation. I. Quasi-static testing. Journal of Polymer Science B Polymer Physics 43, 1794–1811 (2005).
65. Tandon N et al. Electrical stimulation systems for cardiac tissue engineering. Nat Protoc 4, 155–173 (2009). [PubMed: 19180087]

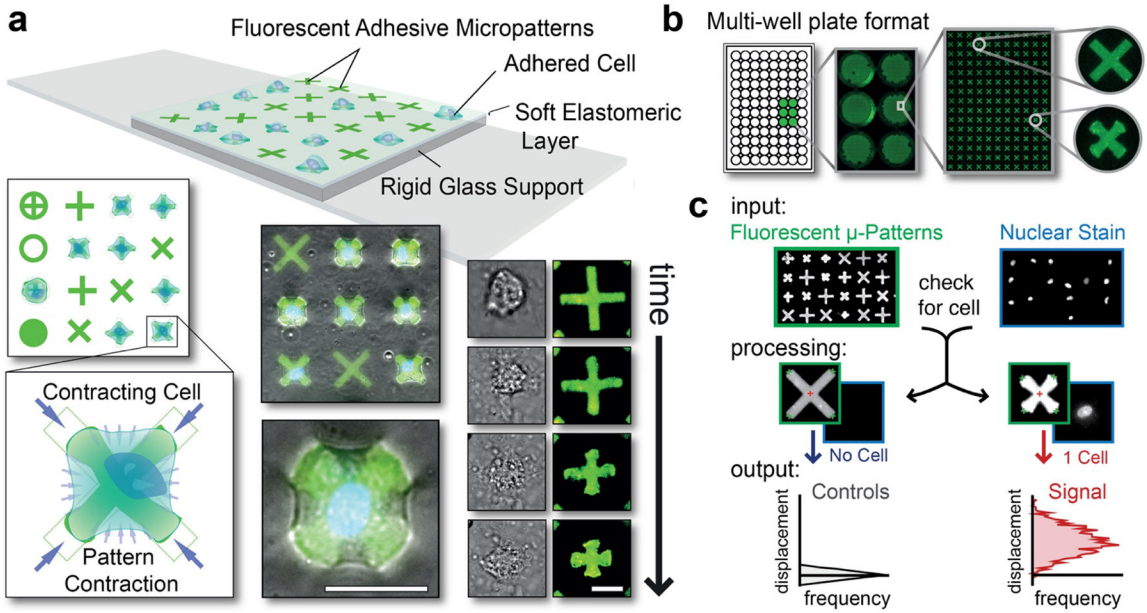

Figure 1: Operational principles of the general-use FLECS force cytometer

(**a**) TOP: Platform schematic showing cells adhered to functionalized adhesive micropatterns embedded into a thin glass-supported elastomeric film. LEFT: Top view showing multiple pattern shapes and a blow-up of a cell contracting an "X" pattern and inwardly displacing its terminals. BOTTOM: Overlay of fluorescent patterns and phase contrast images of adhered contracting cells. RIGHT: Time-lapsed images of a contracting cell and the underlying micropattern. Scale bar represents 25 μm. (**b**) Well-plate implementation. (**c**) Image analysis workflow. INPUT: Image sets of the micropatterns (set 1) and the stained cell nuclei (set 2). PROCESSING: Algorithm (i) identifies and measures all micropatterns in image set 1, (ii) cross-references the positions of each micropattern in image set 2 and (iii) determines whether 0, 1, or >2 nuclei (i.e. cells) are present (see: Fig. S2). OUTPUT: Mean center-to-terminal displacements of the micropatterns containing a single nucleus (i.e. 1 cell) are compared to the median of the corresponding measurement of all un-displaced patterns containing 0 nuclei (i.e. un-occupied patterns) and the differences are plotted as a horizontal histogram.

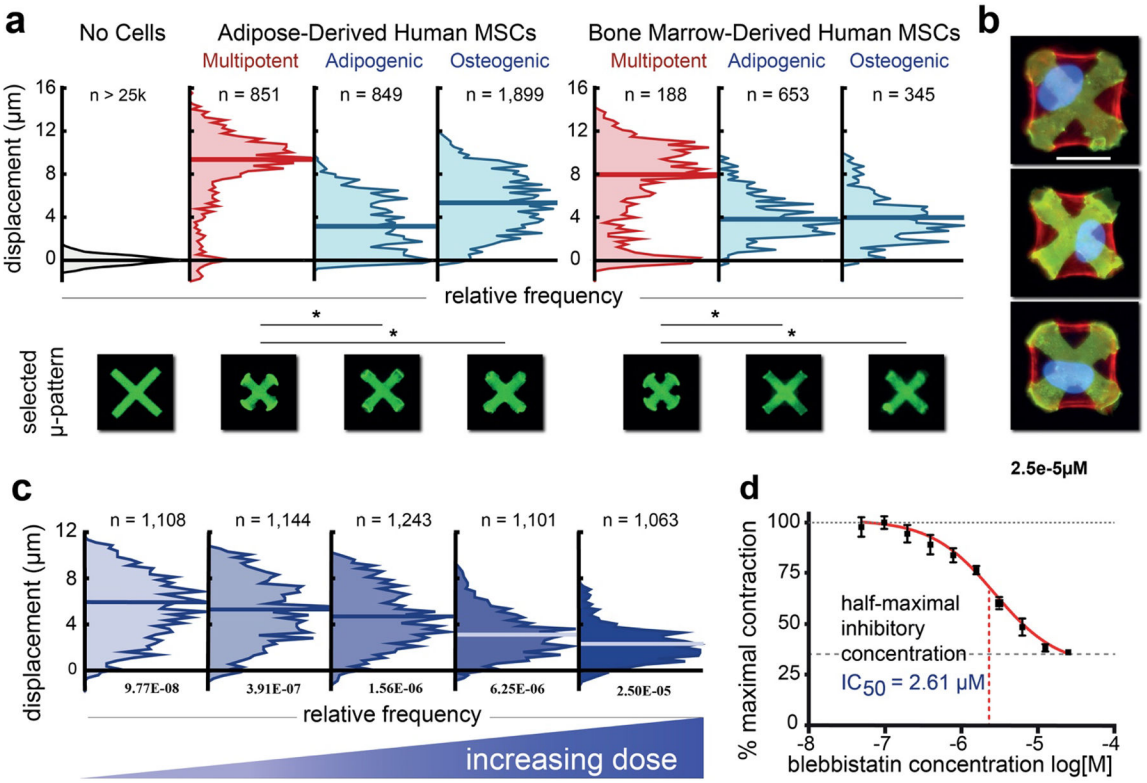

Figure 2: Whole-cell contractility resolves contractile changes with differentiation and drug treatment

(**a**) Primary human adipose- or bone marrow-derived mesenchymal stem cells (MSCs) exhibited much higher contractile responses than either committed lineage 8 hrs post-seeding. Non-contractile subpopulations are seen amongst the MSCs indicating heterogeneity and potentially low purity that results from standard separation methods. N represents the number of cells. A typical contracted pattern representing approximately the median case from each distribution is shown below. (**b**) Overlays of fluorescent images of contracted patterns (green), phalloidin–stained actin (red) and nuclei (blue) of adipose-derived multi-potent MSCs showing three instances of cells fully spread over the patterns and actin stress fibers that route stresses to the vertices of the “X” patterns. Scale bar represents 25 μm. (**c**) Representative distributions of single-cell responses to increasing doses of blebbistatin. Plots comprise pooled data from 4 technical replicates of each condition. (**d**) Dose-response curve over 3 decades in which we identify an IC_{50} of 2.61 μM. Error bars represent SEM. N represents number of cells in each distribution. The Kruskal-Wallis test for non-parametric data was used to perform statistical analysis on the contractile distributions with significance defined as $P < 0.05$.

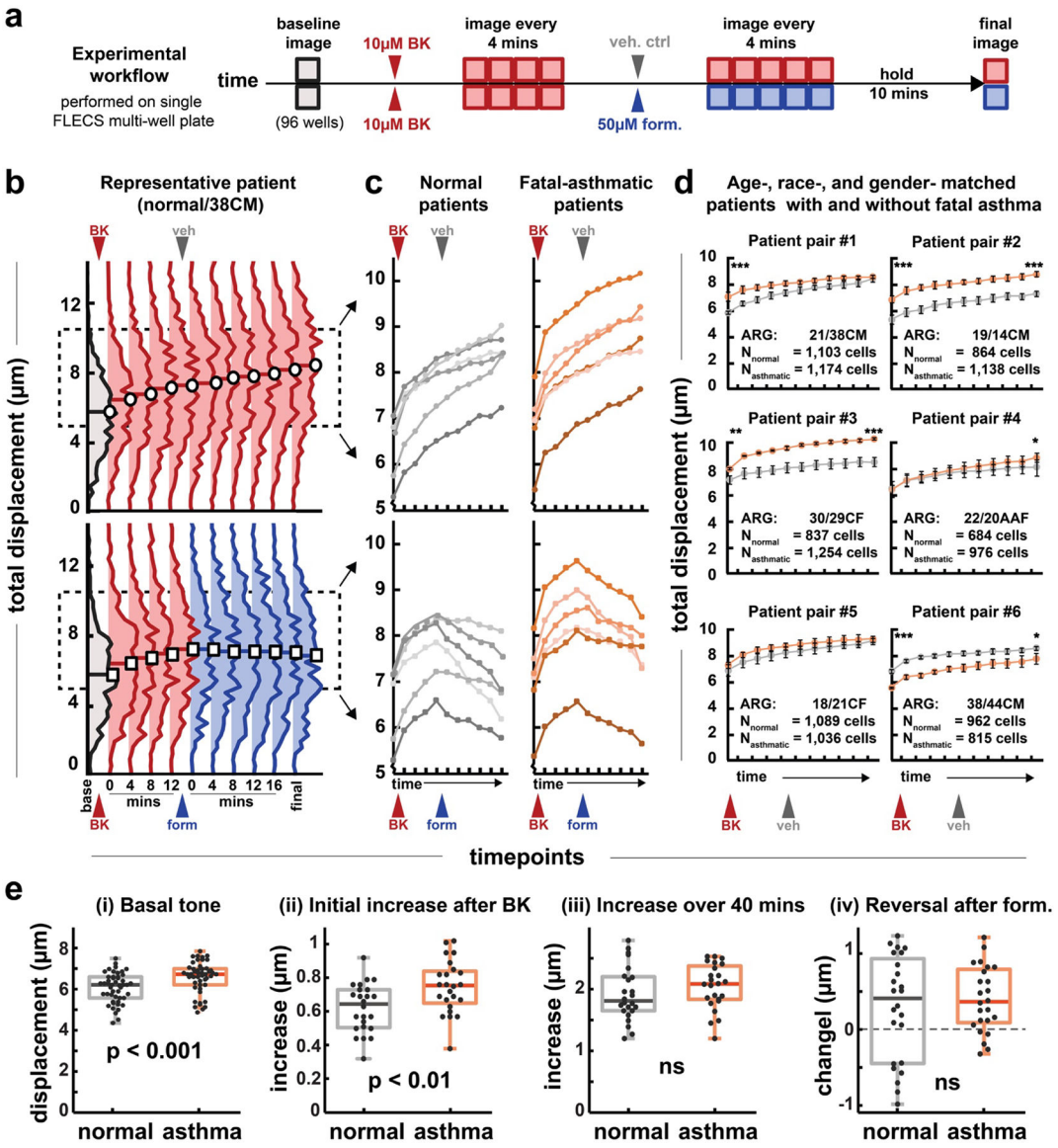

Figure 3: Parallel study of fatal asthma and non-asthma patient-derived airway smooth muscle cells

(**a**) Experimental workflow. 12 patient derived HASM cell lines were seeded into 8 wells each in a FLECS well-plate. A baseline image is taken. Cells are then all treated with the contractile agonist bradykinin (BK, 10 μM final concentration) and imaged for 16 minutes at 4 min intervals. Half of all cells are treated with 50 μM formoterol (form) and the other half with DMSO vehicle (veh). Cells are imaged an additional 20 minutes at 4 min intervals and finally at 10 minutes later. (**b**) Distributions of responsive cells from a representative patient. The distribution shifts upward following BK treatment, and is halted by formoterol. (**c**) Median values of the evolving contractile distributions for each of 12 patient cell lines, with or without formoterol treatment. Each data point of each trace comprises an average of 4 separate well measurements on the well-plate (**d**) Pair-wise comparison of age-, race-, and gender- matched patients with and without asthma. The first age listed is for the normal patient, the second for the asthmatic patient. The letters denote race and gender. The full

characteristics for all patient donors are listed in Table S1. In general, HASM cells from asthma patients exhibit greater tone and/or contraction following stimulation. (**e**) Collective comparisons of all asthma vs non-asthma HASM cells. Each data point represents a median value of an individual well measurement. All wells (96) were compared in (i), only wells that received vehicle (48) were compared in (ii)-(iii) and only wells that received formoterol (48) were compared in (iv). Tone was statistically greater for asthmatic HASM. Initial rate of response to BK was greater for asthmatic cells, however, the long-term time response over the course of the experiment was similar for the two groups. Rescue via formoterol was also similar for the two groups. A one-tailed student's t-test was performed on patient pairs in (d) and pooled groups in (e). In (d) * indicates $P < 0.05$, *** indicates $P < 0.001$. Error bars represent S.E.M.

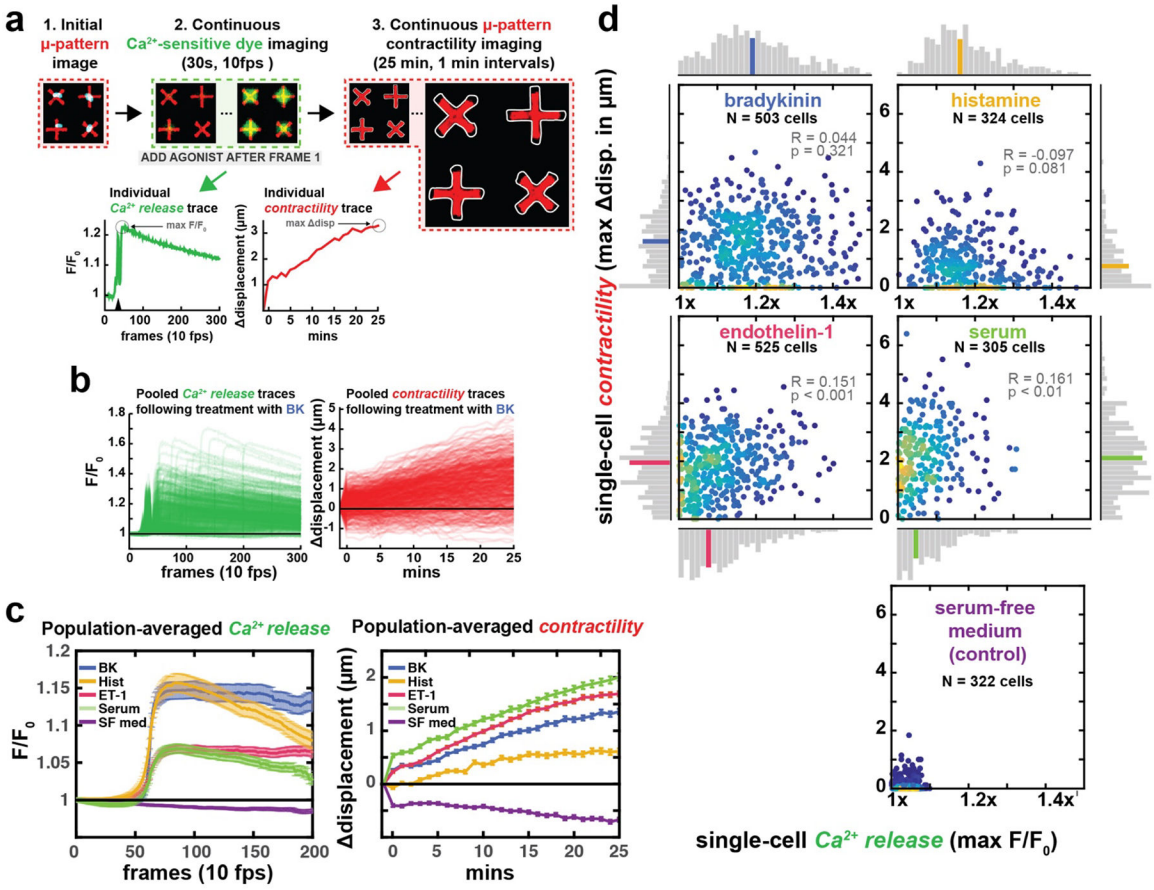

Figure 4: Simultaneous measurements of calcium release and contractility in patient-derived HASM single-cells

(**a**) Experimental workflow. Adhered cells labeled with Fluo-8 are imaged in their tonic state. Agonists are then added and calcium-sensitive dye intensity is recorded for 30s at 100 ms intervals. The same set of micropatterns are then imaged for 25 minutes at 1 minute intervals. Calcium release and contractility traces are extracted from these image series. The black triangle on the individual calcium trace denotes addition of agonist. (**b**) All traces obtained from cells treated with BK, n = 503 cells. (**c**) Population-averaged traces for each agonist. Peak values from the two traces do not correlate, indicating high-intensity calcium signal does not necessarily translate to robust contraction. Error bars represent S.E.M.(**d**) Correlations between peak calcium release and peak contraction for the same single cells. Histograms displayed horizontally and longitudinally correspond to the isolated contractility and calcium measurements, respectively, and the colored bar in each distribution identifies the bin containing the median value. While each agonist induced calcium release and contraction to some extent, we did not observe any strong correlations between these measurements.

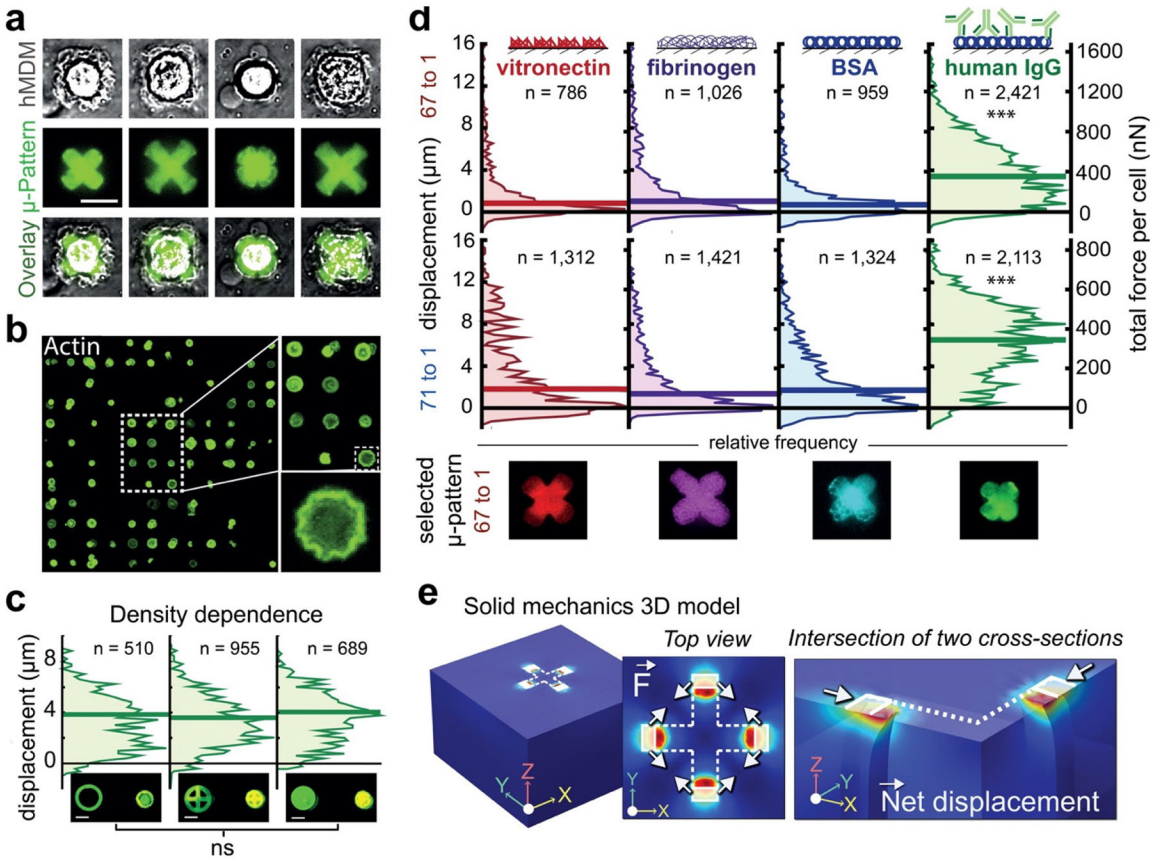

Figure 5: Measuring phagocytic forces generated by individual human macrophages

(**a**) Representative images of hMDMs on hIgG cross patterns showing a range of phagocytic responses. (**b**) Representative image of actin-stained hMDMs spread over circular patterns in an array. High rates of single-cell pattern coverage are achieved. (**c**) Phagocytic contraction of i) ring, ii) cross and iii) filled hIgG circular patterns. The three distributions of single- cell responses were not significantly different. (**d**) Opsonin-dependence in phagocytic contraction. Vitronectin, fibrinogen, BSA, and hIgG were patterned in 50 μm cross shapes on a stiffer, 67:1 base:crosslinker (B:C) (top) and softer 71:1 (bottom) substrate. HIgG elicited the most contractile response from the largest fraction of macrophages, consistent with the role and urgency of antibody opsonization in immunity. Left Y-axis represents displacement in μm; Right Y-axis represents applied forces in nN. A typical pattern representing each distribution in the 67:1 B:C case is shown below. N represents number of cells in each distribution shown in (c) and (d). (**e**) Finite element method modeling of forces exerted by a phagocytosing macrophage. Forces were modeled as boundary loads on a linear elastic material, exerted between all pairs of adjacent terminals of the cross pattern. The shape of the non-displaced pattern is outlined in white and the 5μm by 10 μm area over which force is applied is shaded. LEFT: Complete geometry comprising a 150 μm by 150 μm elastic material with 90 μm thickness. MIDDLE: The top view showing the the direction of applied tangential forces, indicated by the arrows. RIGHT: Cross-sectional view of one quarter of the geometry at 50% opacity highlighting the response of the material to the boundary load and indicating the direction of net displacement. Note: Internal columns of

material are depicted only to emphasize the displaced geometry due to applied forces and do not represent real boundaries in the material. The Kruskal-Wallis test for non-parametric data was used to perform perform statistical analysis on the contractile distributions for the opsonin-dependence experiment, with significance defined as $P < 0.05$. For the density dependence experiment, a one-way ANOVA ruled out any significant differences.

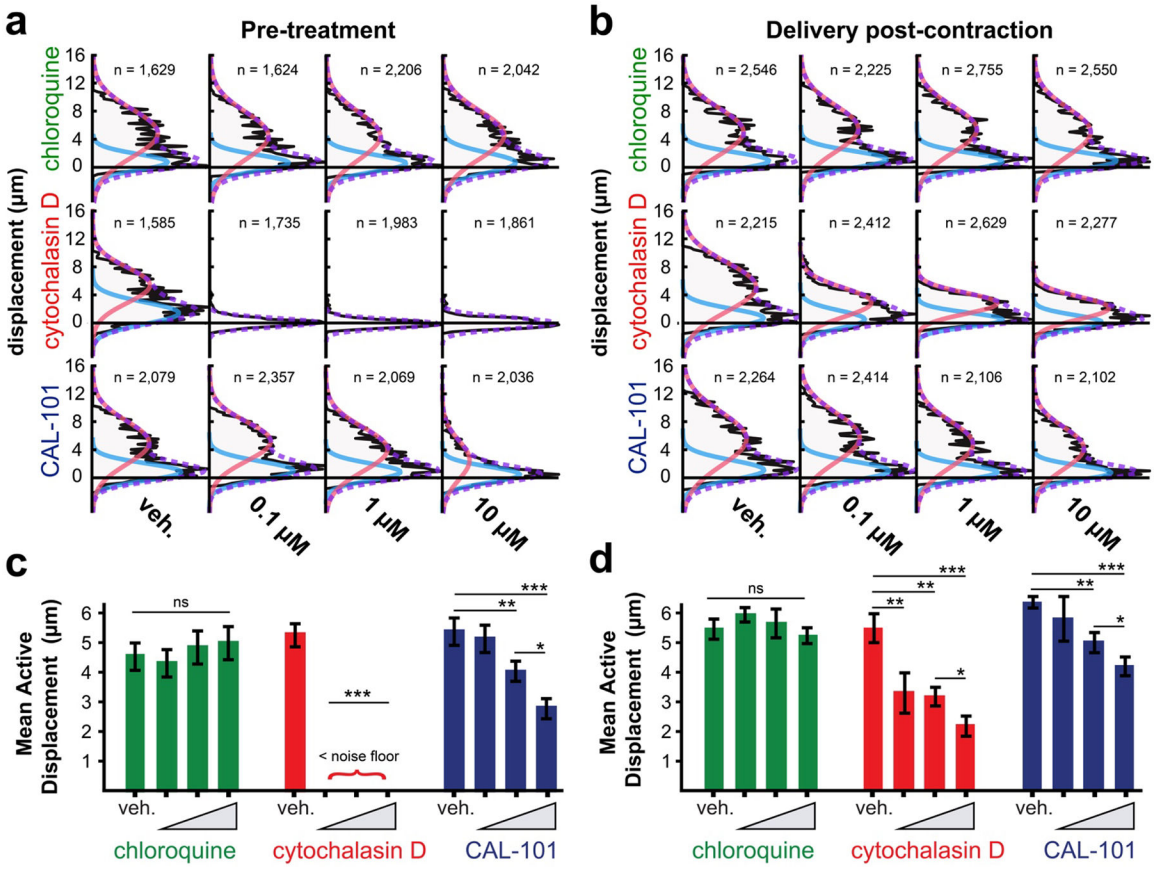

Figure 6: Effects of chloroquine, cytochalasin D and CAL-101 on hMDM contractile force

(**a**) Contraction distributions of hMDMs engaging IgG-opsonized micropatterns pre-treated with DMSO or with three doses of each drug. (**b**) Contraction distributions of hMDMs engaging IgG-opsonized micropatterns incubated with DMSO or with three doses of each drug for 15 minutes after reaching steady-state contraction. In (a) and (b) Data are pooled from 4 technical replicates. A bimodal distribution was observed reflecting an “active” phagocytosing population (red curve) and a weakly adhered, inactive population (blue curve). A mixed Gaussian distribution is fitted to each plot to obtain information about the active populations which is used for quantification. N represents the number of cells in each distribution shown in (a) and (b). (**c**) and (**d**) median contraction levels of the active populations in (a), (b), respectively. Bars represent mean of 4 replicates + SEM. of no treatment and treatment with DMSO control. Measurements were compared using ANOVAs followed by two-tailed Bonferoni corrected t-tests.

Table 1:

Comparison between FLECS and existing methodologies for measuring cellular force

Method	Traction Force Microscopy	Micropost Arrays	FLECS
Fabrication	uses particle mixing with UV- cured gels; micro-contact printing used for uniform single-cell measurements	uses device delamination from molds and functionalization via stamping with protein; micro-contact printing used for uniform single-cell measurements	uses micro-contact printing on sacrificial layer; inherently single-cell
Other Requirements	automated cell detection uses fluorescent tagging of cells;	oil/water-immersion high magnification objectives used[22,45,46]	uses nuclear stain
Image Analysis	user typically defines ROI by manually tracing cells[47–49]; automated cell detection possible with additional cell- labeling procedures[50]	user manually locates cells and 'attached' and 'unattached' posts are identified[13,45,51] automated cell detection possible with additional cell- labeling procedures[22]	micropatterns detected via template-matching algorithm; nuclei counting and micropattern measurements performed using algorithm
Spatial Resolution	sub-cellular	sub-cellular	whole-cell
Time-course	cell migration tracking used if cell not patterned; cells are removed following final time-point to obtain reference	cell migration tracking used if cell not patterned; adhesion/de-adhesion to microposts is tracked	cell locations preserved; no additional action required
Used in Automation Workflow?	bulk-averaged: yes[12] single-cell: not reported	not reported	yes (demonstrated herein)
Data Throughput / Experiment	**typical**: 10–50 cells[11,14,19,20,52] **max reported**: >1000 cells (not single-cell)[12]; ~100 cells (single-cell)[53]	**typical**: ~10–25 cells[15,45,46,51]; **max reported**: ~100 cells[22] (all single-cell)	**typical**: >1000 cells **max reported**: >30^00 cells (all single-cell)
Top Application Areas Explored	bulk-averaged traction moment measurements[12]; mapping complex' subcellular traction forces in individual cells[54] force measurement during cell migration[11,34] correlating traction force with morphology and focal adhesions[20,21,55]	resolving minute sub-cellular differences in related cell types[22]; T-cell force generation[56]; decoupling stiffness from porosity; accurate calculation of absolute force (per micropost)	large count single-cell measurements; rapid time-course for large populations; identification of outliers; co-measurements of phenotypic makers; high-throughput screening;